ORIGINAL RESEARCH

Size-Controlled Preparation and Behavior Study of Phospholipid–Calcium Carbonate Hybrid Nanoparticles

Cheng Wang
Shaoqing Chen
Lu Bao
Xuerong Liu
Fuqiang Hu
Hong Yuan

College of Pharmaceutical Sciences, Zhejiang University, Hangzhou 310058, People's Republic of China

Background: Calcium carbonate (CC) nanoparticles have broad biomedical utilizations, owing to their multiple intrinsic merits. However, bare CC nanoparticles do not allow for the development of multifunctional devices suitable for advanced drug delivery in cancer therapy.

Methods: Phospholipid-modified phospholipid–CC hybrid nanoparticles were prepared in our study using a combination of vapor-diffusion and solvent-diffusion methods to offer optimized pharmaceutical capabilities.

Results: Considering that particle size is a critical parameter that plays an important role in both in vitro and in vivo behaviors of nanoparticles, we here for the first time a present detailed protocol for the size-controlled preparation of hybrid nanoparticles, as well as analysis of the in vitro/in vivo behaviors of differently sized hybrid nanoparticles.

Conclusion: Our results might significantly advance the application of this promising material in more varied fields.

Keywords: calcium carbonate, phospholipid, hybrid nanoparticles

Introduction

Nanotechnology is emerging as a preferable approach in drug delivery (DD).[1,2] Many currently available DD systems (DDSs) are composed of numerous nano-sized particles in which drug molecules can be safely encapsulated and protected from hostile environments.[3,4] As a result, DDSs can offer enhanced stability, bioavailability, and tissue targetability compared to free drugs alone.[5,6] It is well established that calcium carbonate (CC), a naturally atoxic biomineral, has broad biomedical utilizations, owing to its intrinsic advantages of high biocompatibility, low cost, and ease of large-scale production.[7,8] Although numerous DDSs have been developed based on CC nanoparticles, their properties (biological, physical, and pharmaceutical) have not always allowed the development of multifunctional devices suitable for both controlled and targeted DD.[9,10] Therefore, the development of hybrid CC nanoparticles, which raises the possibility of combining advantages of different materials, is becoming an alternative to conventional single systems. Phospholipid (PL) modification has been widely adopted in the construction of many successful DDSs, and offers optimized structural, physical, and pharmaceutical characteristics, along with other merits suitable for application in DD.[11,12]

Correspondence: Hong Yuan
Email yuanhong70@zju.edu.cn

To our limited knowledge, PL-modified CC nanoparticles have rarely been reported in the literature. Few attempts have been made to investigate the effect of different parameters on the formulation of CC-derived nanoparticles. It has been generally recognized that particle size is a critical parameter that plays an important role in both in vitro and in vivo behaviors of nanoparticles.[13] Here, for the first time we report on a detailed protocol for size-controlled preparation of PL–CC hybrid nanoparticles. In our study, preparation of the core–shell hybrid nanoparticles involved two steps. Firstly, CC nanoparticles were synthesized by a vapor-diffusion method. Afterward, the CC nanoparticles obtained were incubated with proper amounts of PL and polyethylene glycol (PEG), followed by a solvent-diffusion method finally to obtain the hybrid nanoparticles.

Methods
Materials
Polyethyleneimine (branched, molecular weight 25,000 Da) was obtained from Sigma-Aldrich (MO, USA). Sodium azide, chlorpromazine, filipin, nystatin, 5-(N-ethyl-Nisopropyl) amiloride (EIPA), cytochalasin D, LysoTracker red DND99, ER Tracker red, tetramethylrhodamine-conjugated human Tfn, Hoechst 33342, and DiR were purchased from Invitrogen (CA, USA) and Solarbio Science and Technology (Beijing, China). The Golgi-pERFP plasmid was a gift form Professor Yingke Xu of Zhejiang University. PL (S100) and 1,2-distearoyl-sn-glycero-3-phosphoethanolamine-N-[methoxy(PEG$_{2,000}$] (DSPE-PEG$_{2,000}$) were offered by Lipoid (Ludwigshafen, Germany) and AVT Pharmaceutical (Shanghai, China). Other reagents were of analytical grade and obtained from Sinopharm Chemical Reagent unless otherwise stated.

Cell Culturing
NIH3T3 (mouse embryonic fibroblast), MCF7 (human breast carcinoma), and L02 (human normal hepatocyte) cell lines were obtained from the Institute of Biochemistry and Cell Biology (Shanghai, China) and cultured in DMEM (Thermo Fisher Scientific) supplemented with FBS 10% v:v (Thermo Fisher Scientific), penicillin (100 U/mL), and streptomycin (100 μg/mL) in a humidified CO_2 incubator (Forma 311; Thermo Fisher Scientific) in 95% air–5% CO_2 at 37°C.

Multicellular Tumor–Spheroid Model
Eestablishment of the multicellular tumor–spheroid (MCTS) model followed the protocols in our previous report.[14] In brief, agarose was autoclaved and added to 96-well plates (Corning, USA) to form gel pads at the bottom of the wells. Afterward, amixed solution of MCF7 and NIH3T3 cells (1:1) was seeded (2×10^3 cells per well) and allowed to incubate for another 4 days to form MCTSs.

Animal Model
Female BALB/c nude mice and New Zealand rabbits were offered by the Shanghai Laboratory Animal Center (SLAC, China) and housed in specific pathogen–free conditions with free access to food and water. To obtain MCF7 tumor–bearing mice, the PBS suspension of MCF7 (2×10^6) cells was subcutaneously inoculated in the flanks of nude mice and allow to grow into solid tumors.[15] All animal experiments were supervised and approved by the Animal Care and Use Committee of Zhejiang University and strictly adhered to the NIH guidelines for care and use of animals.

Synthesis of Calcium Carbonate Nanoparticles via Vapor-Diffusion Method
$CaCl_2$ was firstly dissolved in a small amount of water and then diluted with 50 mL absolute ethanol. The mixture was transferred to another glass bottle, followed by sealing with parafilm (left with several pores for gas exchange). Afterward, the bottle was placed in a desiccator with another two bottles of $(NH_4)_2CO_3$ at a designated temperature. After vapor-diffusion reaction for predetermined time intervals, the mixture was centrifuged at 8,000 rpm for 10 minutes (Allegra 64R; Beckman Coulter, USA) to obtain products. Nanoparticles collected were rinsed several times, redispersed in absolute ethanol, and stored at 4°C.

Preparation of Phospholipid–Calcium Carbonate Hybrid Nanoparticles via Solvent-Diffusion Method
Formulation 2 (F2; average size 70.4±5.86 nm), F10 (average size 187±5.86 nm) and CC nanoparticles sized 248 ±7.23 nm (F21, temperature 30°C, time 24 hours, $CaCl_2$ 100 mg, water content 1.8%) were selected as cores for the

preparation of PL–CC hybrid nanoparticles. The CC nanoparticles, PL (weight:weight ratios of PL:CC nanoparticles 0.5, 1, and 2), and DSPE-PEG (weight:weight ratio of DSPE-PEG:PL fixed at 0.2) were dispersed in mixed solution (2 mL) of ethanol and chloroform (1:1, v:v). The mixture was agitated at room temperature overnight and then subjected to probe sonication (400 W, work 2 seconds after 3 seconds of standing, repeated for 30 cycles). Afterward, the mixture was transferred into a round-bottomed flask and rotary-evaporated, followed by vacuum desiccation. The film formed on the flask wall was again dissolved using absolute ethanol and the solution injected at a constant rate into 18 mL water under stirring via injection syringe. After stirring for 10 minutes at room temperature, the resulting solution was centrifuged (3,000 rpm, 10 minutes) to remove large aggregates (if any) and the supernatant separated and stored at 4°C for further use.

Characterization of Nanoparticles

The size and ζ-potential of nanoparticles were determined with a Zetasizer (Nano ZS90; Malvern, UK). The morphology of nanoparticles was observed using TEM (JEM-1200; JEOL, Japan). The structural formation of hybrid nanoparticles was verified by Fourier-transform infrared spectroscopy (FTIR; FT/IR-4100; Jasco, Japan). The X-ray powder diffraction (XRD) spectrum of hybrid nanoparticles was recorded using a Rotaflex RU-200 (Rigaku, Japan).

In Vitro Cellular Uptake, Excretion, and Endocytosis Pathways

FITC-labeled octadecylamine (FITC-ODA) was synthesized using protocols reported previously[16] and was employed to be a fluorescence marker. To construct the FITC-labeled hybrid nanoparticles, FITC-ODA (weight: weight ratio of FITC-ODA:PL fixed at 0.05, molar ratio approximately of 0.047) was additionally added to the nanoparticles. To investigate the intracellular uptake of different nanoparticles, MCF7 cells were placed in a six-well plate (10^5 cells/well; Corning) and cultured to reach 80%–90% confluence. Afterward, media were discarded and serum-free medium with differently sized hybrid nanoparticles added (20% volume of total medium, with a final nanoparticle concentration of 0.5 mg/mL). At predetermined time intervals, cells were rinsed thoroughly with PBS. Subsequently, cells were detached and lysed with RIPA solution (Solarbio). The solution obtained was subjected to fluorescence measurement using fluorescence spectrophotometer (Ex: 496, Em: 523, slit: 5 nm; F-2500; Hitachi, Japan). The FITC concentration in each group was normalized using a BCA protein-quantification kit (Solarbio) according to the manufacturer's protocols.

To investigate the excretion of nanoparticles, cells were firstly treated with differently sized hybrid nanoparticles for 24 hours. Afterward, culture media were replaced with fresh serum-free ones and continued to incubate for 8 hours. At different intervals, culture media and cells were collected and FITC concentrations within determined using the aforementioned protocol. To evaluate the endocytosis pathways of nanoparticles, cells were treated with designated concentrations of different inhibitors for 30 minutes prior to nanoparticle addition.[17] At 2 hours post-incubation, cells were processed and subjected to fluorescence measurement.

Intracellular Organelle Localization

To visualize lysosome localization, cells were placed in a confocal dish (35 mm; Corning) at a density of 5×10^5 cells/mL and allowed to grow overnight. Afterward, cells were treated with different hybrid nanoparticles and incubated for another 4 hours. Then, cells were labeled with LysoTracker Red DND99 dye (100 nM)–Hoechst33342 (10 µg/mL) for 10 or 30 minutes and observed by confocal laser-scanning microscopy (CLSM; BX61W1-FV1000; Olympus, Japan). To visualize endosome localization, MCF7 cells were firstly incubated with serum-free medium containing tetramethylrhodamine-conjugated human Tfn (40 µg/mL) for 30 minutes. Afterward, differently sized hybrid nanoparticles were added and incubated for another 4 hours and then subjected to CLSM observation. To visualize endoplasmic reticulum (ER) localization, MCF7 cells were incubated with differently sized hybrid nanoparticles for another 4 hours labeled with ER Tracker red (1 µM) for 30 minutes, and then subjected to CLSM observation. To investigate Golgi-apparatus localization, MCF7 cells were firstly transfected with a Golgi–pERFP plasmid using polyethyleneimine 25 kDa as previously reported.[18] Afterward, differently sized hybrid nanoparticles were added and incubated for another 4 hours and then observed with CLSM.

Penetration of Nanoparticles

MCTSs were treated with the different FITC-labeled nanoparticles for 24 hours. Afterward, the MCTSs was washed with PBS and fixed by paraformaldehyde. The penetration

of different nanoparticles was obtained by tomoscan (Z-stack imaging) from the top to the middle using CLSM.

In Vivo Tissue Distribution

DiR-labeled nanoparticles were prepared using the same protocol as the FITC-labeled nanoparticles. Subsequently, different DiR-loaded hybrid nanoparticles were intravenously administered to tumor-bearing nude mice (50 μg DiR/kg). At 6 and 12 hours postadministration, fluorescent images were obtained using an in vivo image–formation system (Maestro, USA). Finally, mice were killed to harvest viscera and tumors, followed by ex vivo imaging with the same system.

Safety Tests

MCF7 and L02 cells were cultured in 96-well plates ($2×10^3$ cells/well; Corning) and allowed to grow to 60% confluence. Afterward, cells were cultured with fresh serum-free medium containing different nanoparticles (10–200 μg/mL) for 48 hours and then subjected to standard MTT assays. For hemolysis assays, different concentrations of nanoparticles were incubated with 2% red blood cell (from New Zealand rabbits) suspensions and maintained at 37°C for 1 hour. Afterward, all samples were centrifuged (3,000 rpm for 10 minutes) to collect the supernatant, absorption of which at 545 nm was determined by ultraviolet spectrophotometry (TU-1810; Persee, China).[19] A total of 24 BALB/c nude mice were grouped randomly (n=6) and administered saline (control) and different nanoparticles (100 mg/kg) every 2 days seven times via tail-vein injections. Variations in body weight were recorded before injections and plotted against time. Finally, mice were killed to collect blood and main organs. Liver and renal functions were assessed and histological H&E analysis conducted.

Statistical Analysis

Results are shown as SD for three parallel experiments. Statistical significance was tested with two-tailed Student's *t*-test or one-way ANOVA, with $P<0.05$ as statistically significant.

Results and Discussion
Single-Factor Study of CC Nanoparticles

The vapor-diffusion method using ethanol as reaction medium was adopted in our study to synthesize CC nanoparticles. In detail, $CaCl_2$ was firstly dissolved in a small amount of water and then diluted with a large amount of absolute ethanol. The mixture was transferred to another glass bottle, followed by sealing with parafilm (left with several pores for gas exchange). Afterward, the bottle was placed in a desiccator with another two bottles of $(NH_4)_2CO_3$ at a designated temperature. During the vapor-diffusion process, the $(NH_4)_2CO_3$ powder decomposed into NH_3 and CO_2, which redissolved in the water of the reaction medium. The regenerated $(NH_4)_2CO_3$ reacted with $CaCl_2$ via an ion-exchange process to form CC particles. The size of the as-prepared CC nanoparticles varied according to many parameters (Tables 1–4), whichare graphed in Figure 1. The influence of temperature on particle size is shown in Figure 1A. From 20°C to 35°C, particle size increased from 51.5 nm (F1) to 91.6 nm (F4), which might have been due to a temperature-increased reaction rate.[20] However, higher temperature (>35°C, F5) might have induced accelerated volatilization of CO_2 from the reaction medium that in turn reduced the concentration of CO_3^{2-} to finally diminish the

Table 1 Sing le-factor Investigation of Temperature

	Temperature (°C)	Time (hours)	CaCl₂ (mg)	Water content (%, v:v)
F1	20	24	100	0.4
F2	25	24	100	0.4
F3	30	24	100	0.4
F4	35	24	100	0.4
F5	40	24	100	0.4

Table 2 Sing le-factor Investigation of Time

	Temperature (°C)	Time (hours)	CaCl₂ (mg)	Water content (%, v:v)
F6	30	6	100	0.4
F7	30	12	100	0.4
F8	30	24	100	0.4
F9	30	36	100	0.4
F10	30	48	100	0.4

Table 3 Single-factor Investigation of CaCl₂ charged weight of CaCl₂

	Temperature (°C)	Time (hours)	CaCl₂ (mg)	Water content (%, v:v)
F11	30	24	25	0.4
F12	30	24	50	0.4
F13	30	24	100	0.4
F14	30	24	200	0.4
F15	30	24	400	0.4

Table 4 Single-factor Investigation of Water Content in Reaction Medium

	Temperature (°C)	Time (hours)	CaCl$_2$ (mg)	Water content (%, v:v)
F16	30	24	100	0.2
F17	30	24	100	0.4
F18	30	24	100	0.8
F19	30	24	100	1.6
F20	30	24	100	2.0

reaction rate to give reduced particle size. Figure 1B illustrates time-dependent variation inparticle size. It was clear that the size of CC nanoparticles were positively correlated with reaction time. Therefore, it was inferred that the formation of CC nanoparticles occurred over the whole reaction process, during which the initially formed CC

nanoparticles gradually grew as a result of consistent crystal nucleation.[21] Increased reaction time might offer sufficient time for crystal nuclei generated to grow or neighboring particles to unite into larger ones. Moreover, it was interesting to note that ultrasmall particles (<50 nm) could be obtained at the early stage of crystal nucleation, which is beneficial for the development of smaller DDSs for deep tissue penetration.

The relationship between the charged weight of CaCl$_2$ and particle size is shown in Figure 1C. It was observed that changes in particle size by charged weight of CaCl$_2$ were divided into two phases. In the first stage, the size increased with increase in CaCl$_2$ (from 25 mg to 50 mg). Afterward, the reverse tendency appeared as the size decreased with increased CaCl$_2$ (from 75 mg to 400 mg). As one of the reactants, Ca^{2+} concentration played a critical role in
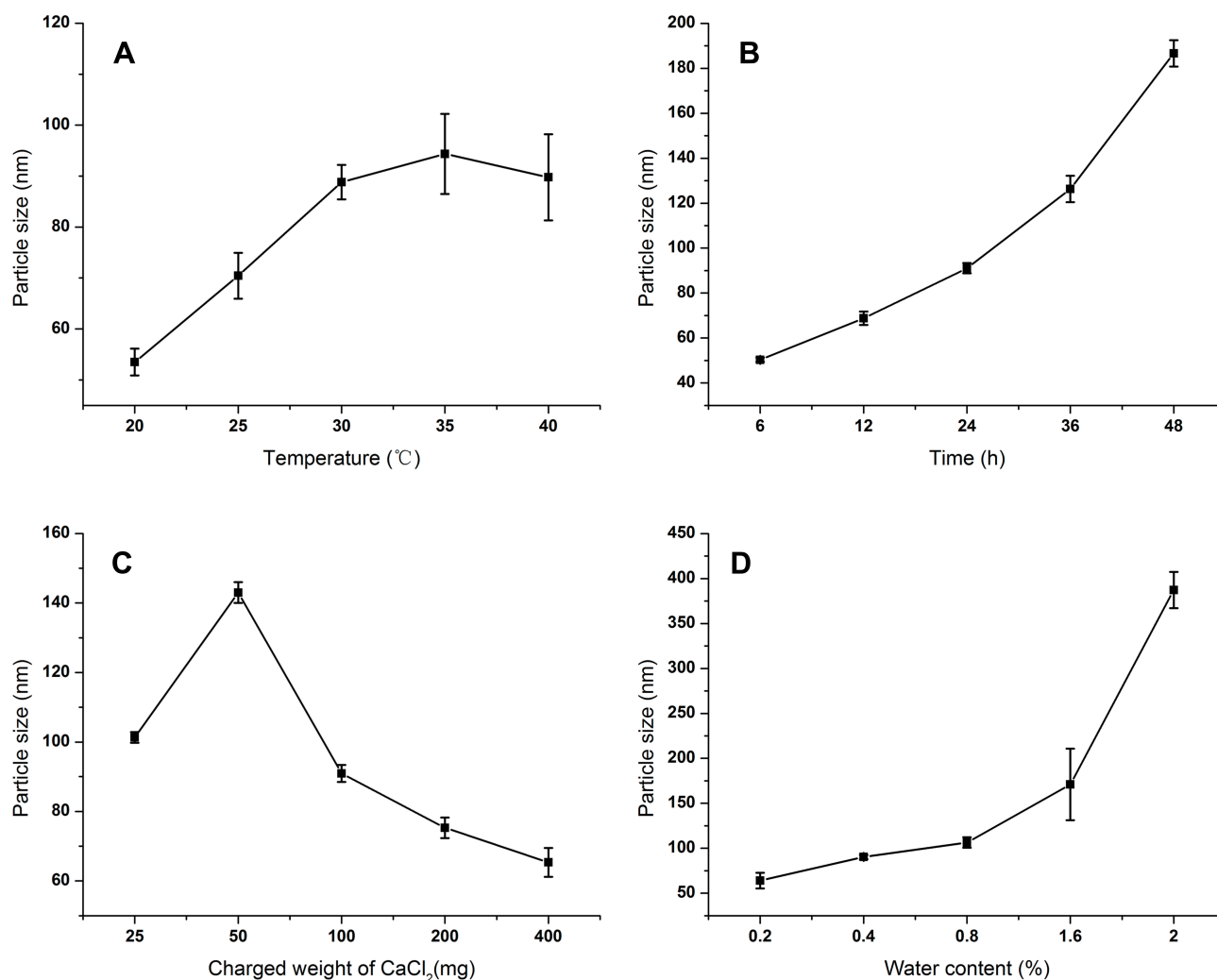

Figure 1 Single-factor investigation on synthesis of CC nanoparticles. (**A**) Temperature; (**B**) time; (**C**) charged weight of CaCl$_2$; (**D**) water content in the reaction medium. Results shown as SD repeated thrice.

determining the size of the resulting CC nanoparticles. It seemed that crystal nucleation and growth were dynamically balanced during the reaction. Under given CO_2 concentrations, the CO_3^{2-} concentration in the medium was constant. When CO_2 was excessive in the first stage, crystal growth was the dominant process that increased $CaCl_2$, resulting in the generation of larger particles. However, continued increases in $CaCl_2$ (second stage) might have reversed the reaction to be crystal nucleation–dominated and rapidly formed crystal nucleation of CC particles lacked sufficient CO_3^{2-} to grow into large particles, which in turn reduced the size of CC nanoparticles. As illustrated in Figure 1D, the water content in the reaction medium played an important role in the size of CC nanoparticles, since a minor increase in water content (from 1.6% to 2%) significantly increased their size from 171 nm (F19) to 387 nm (F20). Moreover, it was noted that water content >2% usually resulted in quick precipitation of the CC nanoparticles under the given conditions (data not shown). Based on these results, it was inferred that due to the extremely high solubility of NH_3 in water (dissolved NH_3 could be further served as acid acceptor to trap CO_2 and further generate $(NH_4)_2CO_3$ and the slight increase in water content could dramatically boost the formation of CC nanoparticles through enhanced $(NH_4)_2CO_3$ concentration. The rapid growth in CC nanoparticles would result in the formation of large particles that finally precipitated as aggregates.

Preparation of Hybrid Nanoparticles

Figure 2 demonstrates the size change in hybrid nanoparticles as a function of PL:CC nanoparticles w:w) ratios. Three differently sized CC nanoparticle groups (70.4 nm, F2; 187 nm, F10; 248 nm, F21) were selected as the core. In the case of F2 (Figure 2A), it was observed that low PL ratio (0.5) led to increased size of hybrid nanoparticles. Size distribution demonstrated that there were two differently sized particle types in the formulation. One was >1,000 nm, which resulted from the adhesion of CC nanoparticles due to sharing of neighboring PL molecules. Increase of PL ratio to 1 resulted in uniform size distribution at 90.3 nm, which was slightly larger than that of the core (70.4 nm). Further increased ratio (w:w 2) led to PL redundancy, which formed additional small nanostructured lipid carriers at around 30 nm. The other two CC nanoparticle types showed similar tendencies. In detail, low PL ratio (0.5) resulted in both larger nanoparticles (>1000 nm) in both F10 (Figure 2B) and F21 (Figure 2C), while high PL ratio (2) created additional nanostructured lipid carriers sized <100 nm. These results demonstrated that PL might have anchored to the shell of CC nanoparticles to generate hybrid nanoparticles. Considering the results given in Figure 2, nanoparticles adopted in the following studies were all prepared at the w:w ratio of 1.

Characterization of Hybrid Nanoparticles

The morphology of obtained CC and hybrid nanoparticles was observed by TEM. As displayed in Figure 3, A–F, all formulations contained numerous spherical, well-separated nanoparticles. Most importantly, the resulting hybrid nanoparticles showed approximate sizes of 100 nm, 200 nm, and 300 nm, and were employed to explore size-dependent in vitro and in vivo behaviors of this platform. The structural formation of hybrid nanoparticles (100 nm) was verified by FTIR (Figure 3G). According to a previous report, the splitting peaks at around 1,417 and 1,474 cm^{-1} were assigned to the asymmetric stretch in carbonate,[22] indicating the existence of CC. Moreover, the characteristics of methylene vibration bands (asymmetric and symmetric) at 2,926 and 2,850 cm^{-1} in pure PL were also observed in PL-modified CC nanoparticles,[23] which suggested that hybrid nanoparticles had been successfully prepared.
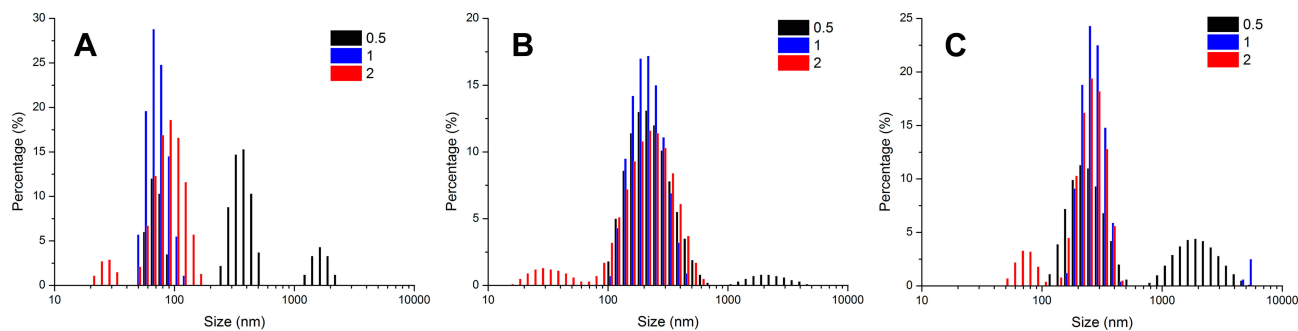

Figure 2 Size variation of hybrid nanoparticles as a function of differently charged ratios (phospholipid:CC, w:w) using differently sized CC nanoparticles as templates. (**A**) 70.4 nm; (**B**) 187 nm; (**C**) 248 nm.
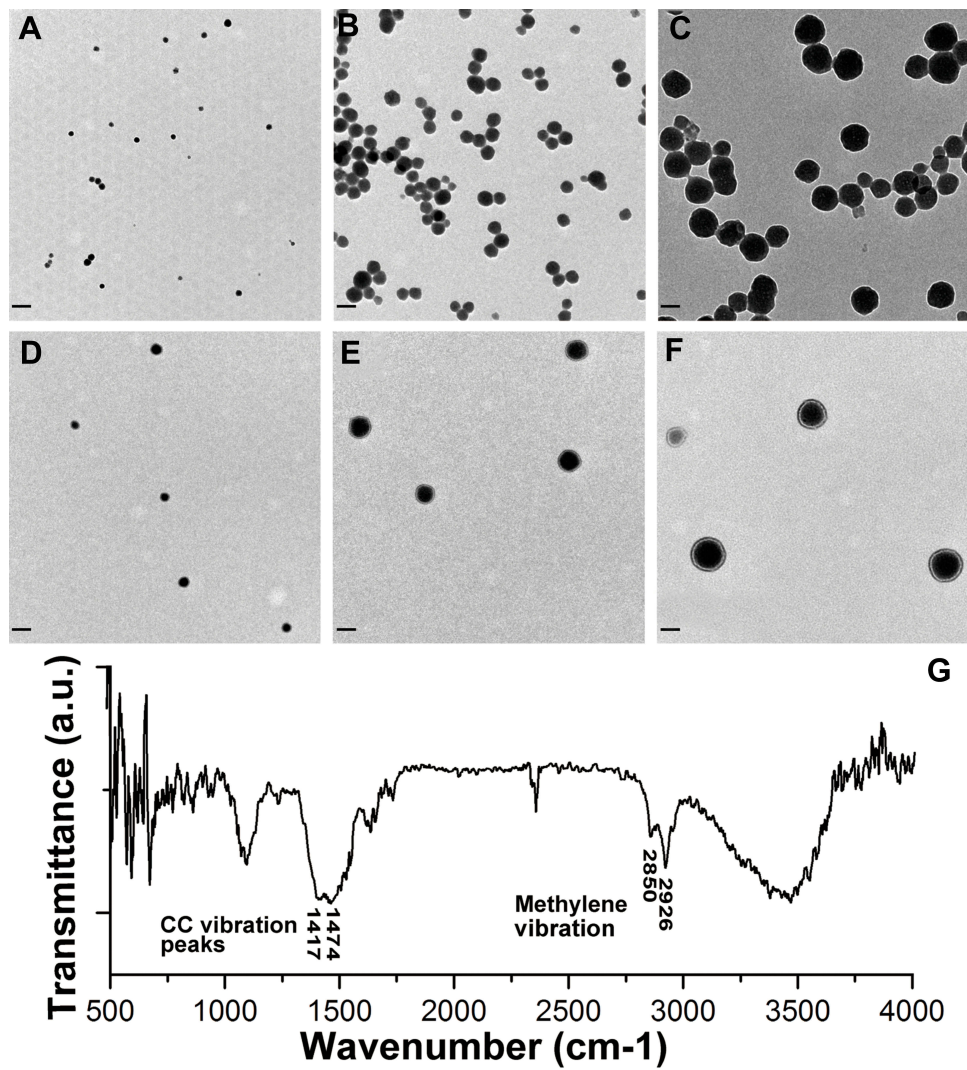
Figure 3 (**A**–**F**) TEM images of differently sized CC (**A** F2; **B** F10; **C** F21) and hybrid nanoparticles (**D** hybrid F2, 100 nm; **E** hybrid F10, 200 nm; **F** hybrid F21, 300 nm). Scale bar 200 nm. (**G**) FTIR spectra of hybrid nanoparticles.
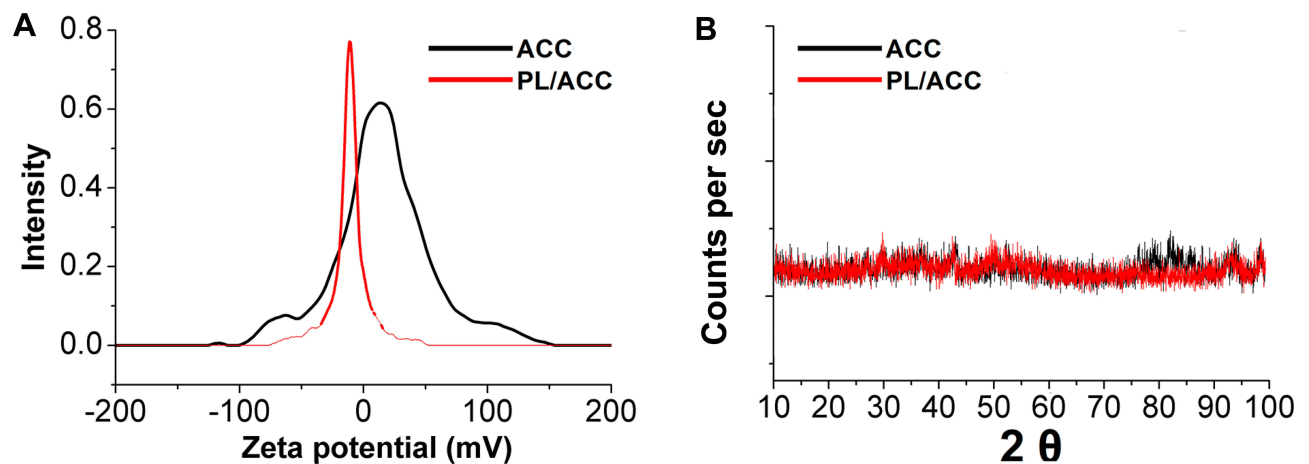

Figure 4 (**A**) ζ-potential of CC (F2) and hybrid nanoparticles (100 nm). (**B**) XRD spectrum of CC (F2) and hybrid nanoparticles (100 nm).

As shown in Figure 4A, CC nanoparticles (F2) were positively charged of 15.96 mV, which might have been due to the excess Ca^{2+} that adsorbed on the surface during the preparation process.[24] However, after surface modification with PL and DSPE-PEG, the surface charge of the resulting hybrid nanoparticles (100 nm) reversed to be −11.87 mV, which suggested the successful deposition of lipids on the surfaces of CC nanoparticles. The XRD spectrum (Figure 4B) revealed that the as-prepared CC nanoparticles (F2) were of amorphous form. Most importantly, the hybrid nanoparticles (100 nm) also preserved the amorphous nature of the CC core, which suggested that the surface-anchored lipid components could offer reliable protection to the CC core.

In Vitro Cellular Uptake, Excretion, and Endocytosis Pathways

The in vitro cellular uptake of different hybrid nanoparticles on MCF7 cells was investigated. As shown in Figure 5A, at merely 2 hours postincubation, an obvious fluorescence signal was detected within the MCF7 cells. Extended incubation until 24 hours showed an increase in fluorescence intensity, suggesting that the cellular uptake of MCF7 cells to the as-prepared hybrid nanoparticles was positively time-dependent. However, it was noted that a significant difference was noted among three hybrid nanoparticle types and uptake efficiency was negatively related to particle size, such that cellular fluorescence intensity in all tested time intervals followed the sequence of 100 nm > 200 nm > 300 nm. PL density might have have played an irreplaceable role in affecting the uptake of nanoparticles, where thinner

ones were more preferably internalized by cells, which deserves to be explored in our future work.

The excretion behavior of different hybrid nanoparticles on MCF7 cells after 24 hours of incubation was also studied. As shown in Figure 5B, the transportation of hybrid nanoparticles in MCF7 was a two-way process. It was observed that excretion of hybrid nanoparticles was also positively time-dependent. In contrast, differently to the significant difference in uptake process, excretion of different hybrid nanoparticles in MCF7 cells was comparable in all three nanoparticle types, with 12%–14% of all nanoparticles being excreted at 8 hours postincubation.

In order to illuminate the endocytosis mechanisms responsible for the significant difference among different nanoparticle types, different inhibitors were adopted. As shown in Figure 6, after treatment with sodium azide, a molecule inhibits energy-dependent transport,[25] and there was an evident drop in uptake in all hybrid nanoparticles: 64.91% (100 nm), 59.51% (200 nm), and 48.81% (300 nm) of control, respectively. This result clearly demonstrated that the endocytosis of hybrid nanoparticles was a highly energy-dependent process. It was also noted that large nanoparticles relied more on energy than small nanoparticles, since the latter might be able to penetrate into cells via other energy-free pathways (such as receptor-mediated diffusion).

Lipid raft/caveolae–mediated endocytosis, clathrin-mediated endocytosis, and micropinocytosis are three main endocytosis pathways being identified for cellular uptake.[26] According to a previous report, lipid rafts/caveolae-mediated endocytosis via either specific or aspecific
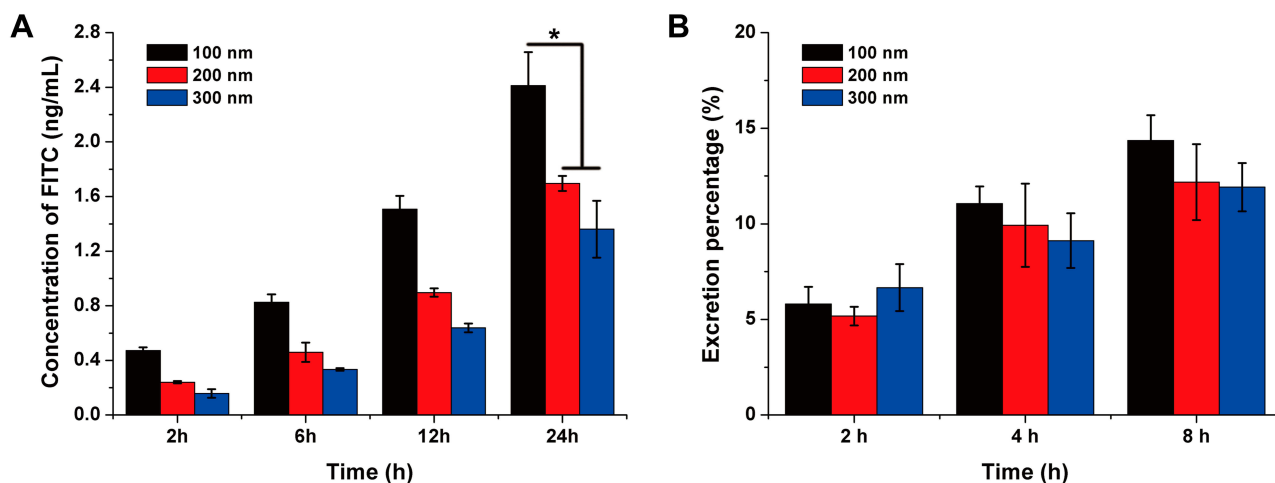

Figure 5 (**A**) Time-dependent endocytosis of different hybrid nanoparticles in MCF7 cells. (**B**) Time-dependent excretion of different hybrid nanoparticles from MCF7 cells after 24 hours' incubation. Results shown as SD repeated thrice. *P<0.05 considered statistically significant.
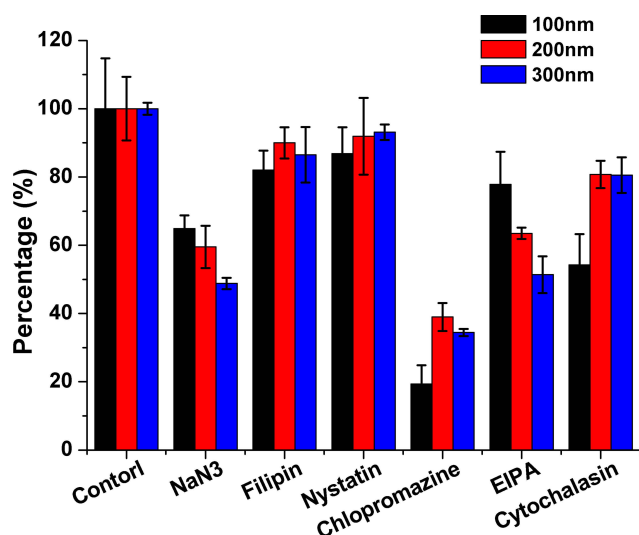
Figure 6 Cellular uptake–mechanism study of different hybrid nanoparticles in MCF7 cells. Results shown as SD repeated thrice.

interactions is responsible for the internalization of many extracellular macromolecules.[27] Herein, filipin and nystatin, as cholesterol binding and sequestering agents, respectively, were adopted in our study. Filipin is the inhibitor to lipid raft/caveolae–mediated endocytosis through competitive binding with cholesterol, while nystatin can trigger the loss of intracellular lipid rafts/caveolae by sequestering cholesterol.[28] The results demonstrated in Figure 6 suggested that both filipin and nystatin showed only a gentle reduction in the endocytosis of hybrid nanoparticles and small particles were more susceptible to inhibition. This was in contrast to our previous study,[17] where endocytosis of lipid nanoparticles was significantly dependent on this pathway, and deserves further investigation.

Moreover, it was demonstrated that chlorpromazine as the inhibitor for clathrin-mediated endocytosis significantly decreased the endocytosis of hybrid nanoparticles, and in particular reduced 80.62% of the uptake of 100 nm nanoparticles. This result indicated that clathrin-mediated endocytosis played a critical role in the endocytosis of hybrid nanoparticles, especially small ones. Therefore, it was inferred that endocytosis of the as-prepared hybrid nanoparticles was mainly regulated by clathrin-coated vesicles.

A commonly used inhibitor for micropinocytosis, EIPA was adopted in our study.[29] As shown in Figure 6, obvious decreases in uptake were observed after EIPA treatment (22.15% for 100 nm, 36.51% for 200 nm, and 48.61% for 300 nm), suggesting that micropinocytosis also exerted a moderate influence on this process. Most importantly, it was observed that the micropinocytosis was positively related to nanoparticle size. It has been reported that particles >150 nm are more prone to be endocytosed through macropinocytosis, which explains perfectly the finding that larger hybrid nanoparticles were more susceptible to EIPA inhibition.[30]

Finally, cytochalasin D was added to explore whether actin was involved in the transportation of hybrid nanoparticles.[31] As illustrated in Figure 6, cytochalasin D inhibition slightly decreased the uptake of large nanoparticles (200 nm and 300 nm), but significantly reduced the percentage of small nanoparticles (100 nm) to 54.27% of untreated cells, which suggested that endocytosis of hybrid nanoparticles depended on actin to some extent, in particular small ones.

In summary, the endocytosis pathways for 100 nm hybrid nanoparticles were more diverse, while larger nanoparticles were tended more to be internalized via clathrin-mediated endocytosis and macropinocytosis. With a direct effect on the fusibility (hence cell uptake) of particles, PL density might also have changed the behavior of nanoparticles, which deserves to be explored in future work.

In order to reveal further organelle distribution of different nanoparticles after endocytosis, intracellular organelle distribution was analyzed. As shown in Figure 7A, all three nanoparticle types merged perfectly with lysosomes, indicating that the following process after endocytosis was mainly dependent on the active transportation of lysosomes, which is consistent with the foregoing conclusion that the endocytosis of hybrid nanoparticles is highly energy-dependent. However, it was noted that large nanoparticles had higher colocation coefficients with lysosomes than small nanoparticlesin line with Figure 6, where large nanoparticles depended more heavily on active energy-dependent transportation.

Furthermore, tetramethylrhodamine-conjugated human Tfn was employed to mark endosomes (Tfn-endosomes) responsible for clathrin-mediated endocytosis[32] and the colocation of different nanoparticles with Tfn-endosomes investigated. As shown in Figure 7B, small nanoparticles demonstrated higher colocation coefficients with Tfn-endosomes than large nanoparticles, which was consistent with the results obtained in the chlorpromazine-inhibition assay.

The ER and Golgi apparatus represent the cytomembrane system, which is responsible for the active transportation of intracellular materials. As displayed in Figure 7, C and D, mass distribution of all three nanoparticle types was observed in both the ER and Golgi apparatus, indicating that
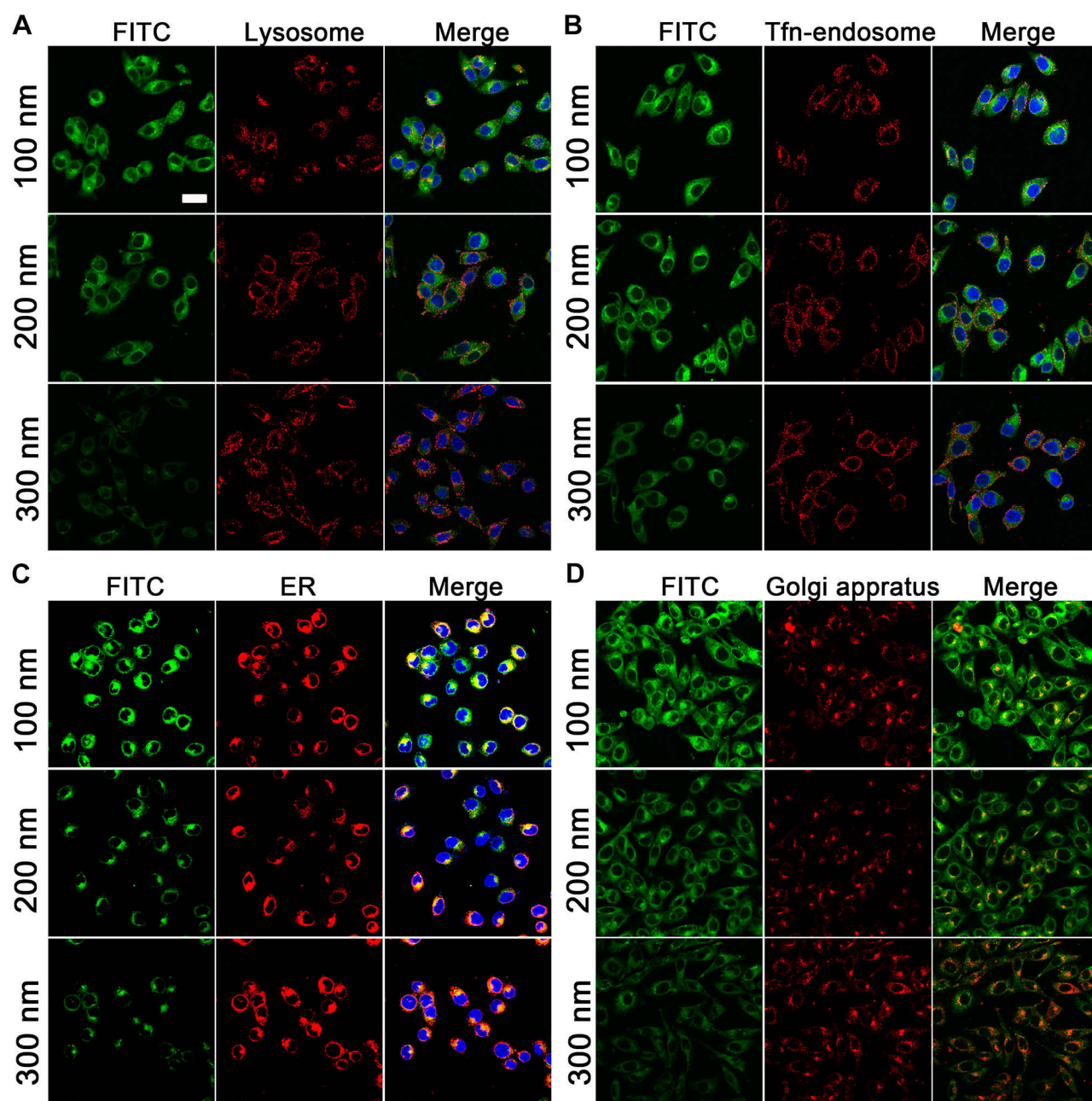
Figure 7 Colocalization of different hybrid nanoparticles with lysosomes (**A**), Tfn-endosomes (**B**), ER (**C**), and Golgi apparatus (**D**) in MCF7 cells at 4 hours postincubation. Scale bar 20 μm. Blue represent location and cell nuclei.

the transportation of hybrid nanoparticles was highly dependent on the cytomembrane system. In addition, it was also foundd that large nanoparticles had higher colocation coefficients with the ER and Golgi apparatus than small ones, similar to lysosome distribution, suggesting that nanoparticles within lysosomes might finally have been transported to the ER and Golgi apparatus for further distribution and metabolism.

Penetration Study

The MCTS model was adopted in our study to simulate solid tumors in vivo, and the penetration capability of different nanoparticle types was studied. As shown in Figure 8, after incubation with different nanoparticle types for 12 hours, FITC fluorescence at different depths of MCTSs was monitored by CLSM. In the 100 nm group, a clear fluorescence signal was obtained at even 120 μm
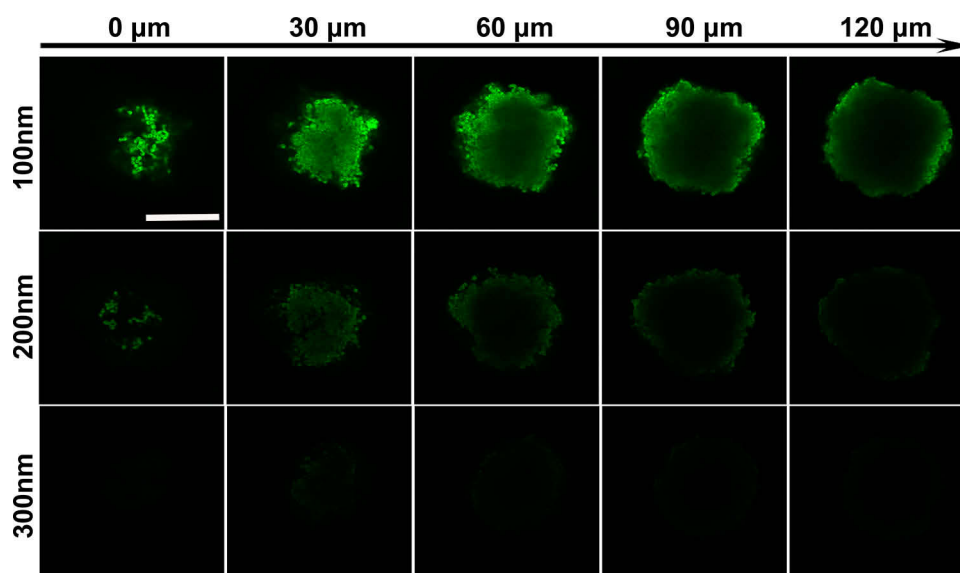
Figure 8 Penetration of different hybrid nanoparticles in MCF7 tumor spheroids. Scale bar 200 μm.

beneath the surface. In comparison, the fluorescence signal in the 200 nm group was greatly attenuated, while there was hardly any signal observed in the 300 nm group at the same depth. As a result, it was clear that the penetration capability of hybrid nanoparticles was negatively related to size, consistent with previous studies.[33,34]

In Vivo Tissue Distribution

To monitor the in vivo tissue distribution of hybrid nanoparticles, the infrared dye DiR was encapsulated in the lipid matrix of hybrid nanoparticles during preparation and the distribution of DiR-labeled nanoparticles was investigated on an MCF7 oxgraft–tumor model. Fluorescence signals were clearly obtained within tumor tissue at 6 hours post injection, and signal intensity increased as time extended (Figure 9A). It was noteworthy that the distribution of hybrid nanoparticles in tumor tissue was negatively related to particle size, which was also confirmed by ex vivo distribution assays. As shown in Figure 9, B and C, the distribution of 100 nm hybrid nanoparticles in tumors was 2.03- and 4.45-fold that of 200 nm and 300 nm ones, respectively. In contrast, the liver/spleen signal of 100 nm hybrid nanoparticles was merely 0.45/0.73- and 0.33/0.23-fold that of 200 nm and 300 nm ones, respectively.

It is generally recognized that size is a key parameter determining the in vivo destiny of nanoparticles.[35] Previous studies have demonstrated that nanoparticles of about 100 nm can preferably evade reticuloendothelial system capture and take advantage of the enhanced penetration and

retention effect in tumor tissue when compared to particles of other sizes, in line with our results.[36,37] Therefore, it was inferred that the as-prepared 100 nm hybrid nanoparticles achieved satisfactory tumor-homing results to reduce unwanted distribution in other organs, which is beneficial to increase bioavailability and reduce drug-related side effects and serves as a promising DDS for advanced cancer therapy.

Safety Tests

To explore the safety profile of hybrid nanoparticles, hemolysis of different concentrations of nanoparticles was carried out. As shown in Figure 10A, no hybrid nanoparticles showed any apparent hemolysis (<1.5%) even at a concentration of 2 mg/mL. Considering the actual nanoparticle concentration would be much lower than our tested ones, it was thus concluded that the as-prepared hybrid nanoparticles inherited no hemolysis risk.[38] The cytotoxicity of hybrid nanoparticles to both normal (L02) and neoplastic (MCF7) cells was also investigated. As displayed in Figure 10B, cell viability of both cell lines all exceeded 95% at all tested concentrations, suggesting that the as-prepared hybrid nanoparticles showed negligible cytotoxicity.

To evaluate whether the hybrid nanoparticles would cause any side effects in treatment, healthy mice were continuously subjected to intravenous injection of hybrid nanoparticles (seven times). Their body-weight variation in comparison to untreated ones was recorded. As shown in Figure 10C, the body weight of all recipients showed insignificant changes
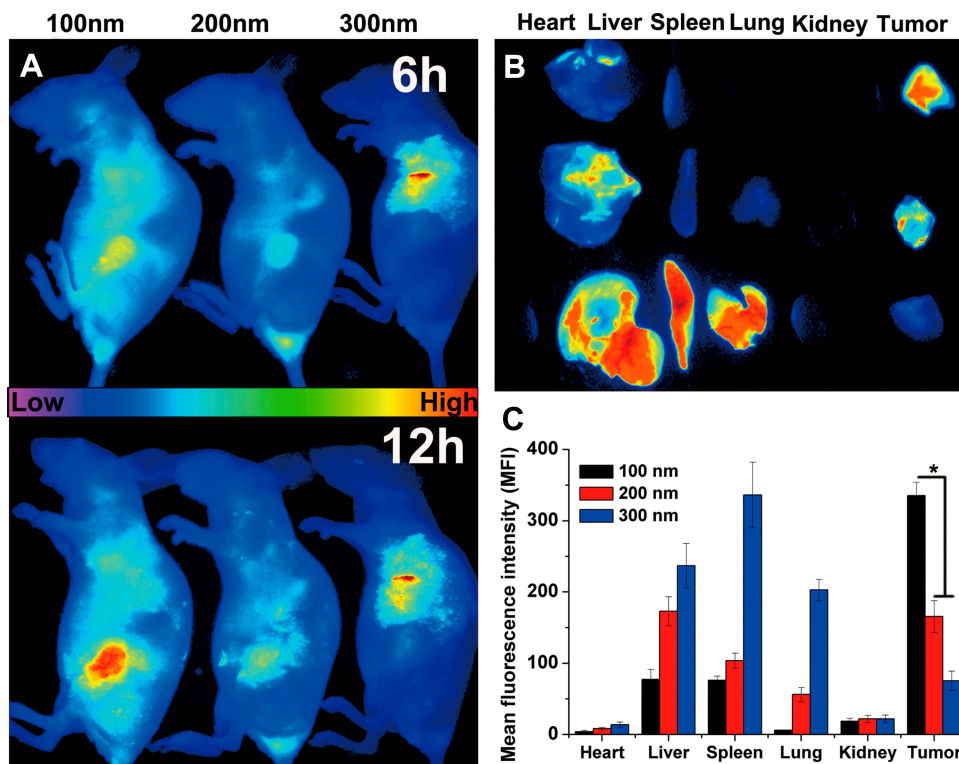
Figure 9 In vivo biodistribution of DiR-loaded hybrid nanoparticles. (**A**) Fluorescence images of time-dependent (6 and 12 hours) distribution of nanoparticles in MCF7 tumor–xenograft mice. Ex vivo images (**B**) and semiquantitative analysis (**C**) of main viscera and tumors at 12 hours after injection. Results shown as SD repeated thrice. *P<0.05 considered statistically significant.

compared to those in the saline group, which suggested that their health quality was not affected. In order to reveal further the health condition of the mice, indicators for renal function (creatinine, total proteins, and urea nitrogen in blood) and biomarkers for liver function (alanine aminotransferase,

alkaline phosphatase, and total bilirubin) were tested.[39] As shown in Figure 10, D–I, hybrid nanoparticles showed similar results to the saline group, suggesting negligible nephrotoxicity and hepatotoxicity. Finally, the main organs were also harvested for histopathological investigation. As shown in
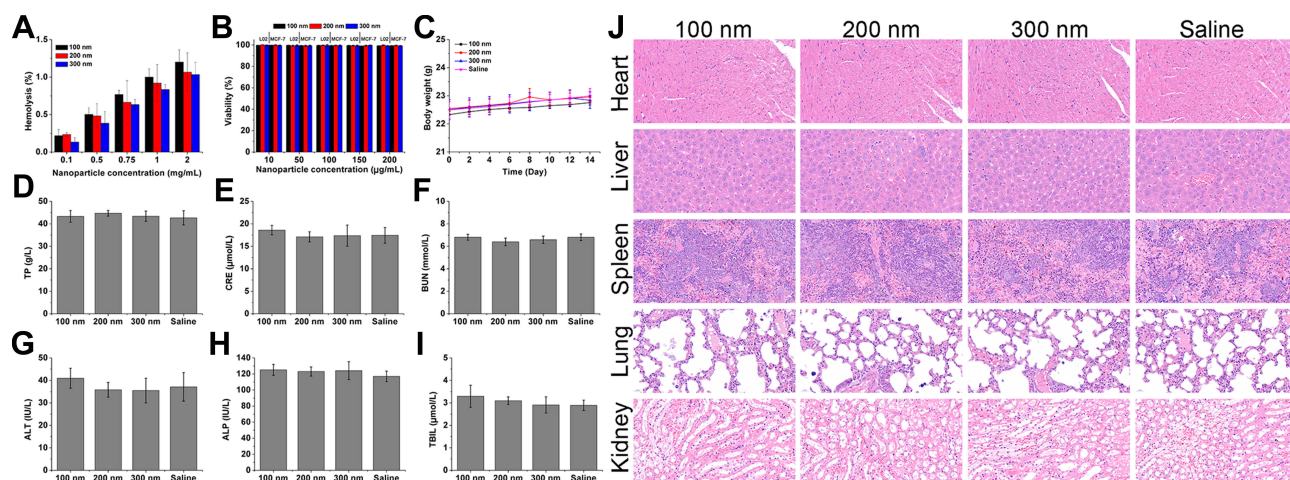

Figure 10 Safety tests of different hybrid nanoparticles. (**A**) Hemolysis of 2% red blood cells treated with various concentrations of hybrid nanoparticles for 1 hour. (**B**) Cytotoxicity of L02 and MCF7 cells treated with different concentrations of hybrid nanoparticles for 48 hours. (**C**) Body-weight variations of mice intravenously administered with different hybrid nanoparticles seven times in 14 days (dosage 10 mg/kg). (**D–I**) Investigation of renal function–related parameters (TP, Cre, and BUN) and liver function–related parameters (ALT, ALP, and TBil) of recipients at the end of administration. (**J**) H&E histopathological sections (200×) of major organs harvested from recipients at the end of administration. Results shown as SD repeated thrice.

Figure 10J, similarly to saline group, no apparent organic damage associated with nanoparticle toxicity were noted in hybrid nanoparticle–treated groups.

Conclusion

In summary, the size of as-prepared CC nanoparticles using the vapor-diffusion method was affected by temperature, time, charged weight of $CaCl_2$, and water content in the system. The size of the hybrid nanoparticles depended on the charged weight of PL. In MCF7 cells, smaller hybrid nanoparticles showed faster cellular uptake, while excretion of all three hybrid nanoparticles was similar. Endocytosis pathways for 100 nm hybrid nanoparticles were more diverse, while larger nanoparticles tended to be internalized more by clathrin-mediated endocytosis and macropinocytosis. Furthermore, our data also revealed that smaller hybrid nanoparticles showed deeper penetration into MCTSs with superior tumor-homing capabilities. The hybrid nanoparticles showed almost no cytotoxicity in vitro or in vivo and had high biocompatibility, which could marke them as a potential candidate for DD to meet various demands.

Acknowledgment

Disclosure

The authors report no conflicts of interest in this work.

References

1. Farooq MA, Aquib M, Farooq A, et al. Recent progress in nanotechnology-based novel drug delivery systems in designing of cisplatin for cancer therapy: an overview. *Artif Cells Nanomed Biotechnol.* 2019;47 (1):1674–1692. doi:10.1080/21691401.2019.1604535
2. Love JC, Estroff LA, Kriebel JK, Nuzzo RG, Whitesides GM. Self-assembled monolayers of thiolates on metals as a form of nanotechnology. *Chem Rev.* 2005;105(4):1103–1170. doi:10.1021/cr0300789
3. Sahoo SK, Labhasetwar V. Nanotech approaches to drug delivery and imaging. *Drug Discov Today.* 2003;8(24):1112–1120. doi:10.1016/S1359-6446(03)02903-9
4. Shi J, Votruba AR, Farokhzad OC, Langer R. Nanotechnology in drug delivery and tissue engineering: from discovery to applications. *Nano Lett.* 2010;10(9):3223–3230. doi:10.1021/nl102184c
5. Kakkar A, Traverso G, Farokhzad OC, Weissleder R, Langer R. Evolution of macromolecular complexity in drug delivery systems. *Nat Rev Chem.* 2017;1(8):0063. doi:10.1038/s41570-017-0063
6. Mitchell MJ, Jain RK, Langer R. Engineering and physical sciences in oncology: challenges and opportunities. *Nat Rev Cancer.* 2017;17 (11):659. doi:10.1038/nrc.2017.83
7. Wang C, Chen S, Wang Y, et al. Lipase-triggered water-responsive "Pandora's Box" for cancer therapy: toward induced neighboring effect and enhanced drug penetration. *Adv Mater.* 2018;30:1706407. doi:10.1002/adma.201706407
8. Wang C, Chen S, Yu Q, Hu F, Yuan H. Taking advantage of the disadvantage: employing the high aqueous instability of amorphous calcium carbonate to realize burst drug release within cancer cells. *J Mater Chem B.* 2017;5(11):2068–2073. doi:10.1039/C6TB02826H
9. Svenskaya Y, Parakhonskiy B, Haase A, et al. Anticancer drug delivery system based on calcium carbonate particles loaded with a photosensitizer. *Biophys Chem.* 2013;182:11–15. doi:10.1016/j.bpc.2013.07.006
10. Zhao D, Zhuo R-X, Cheng S-X. Alginate modified nanostructured calcium carbonate with enhanced delivery efficiency for gene and drug delivery. *Mol Biosyst.* 2012;8:753–759. doi:10.1039/C1MB05337J
11. Li J, Chen Y-C, Tseng Y-C, Mozumdar S, Huang L. Biodegradable calcium phosphate nanoparticle with lipid coating for systemic siRNA delivery. *J Control Release.* 2010;142:416–421. doi:10.1016/j.jconrel.2009.11.008
12. Semalty A, Semalty M, Rawat BS, Singh D, Rawat MSM. Pharmacosomes: the lipid-based new drug delivery system. *Expert Opin Drug Deliv.* 2009;6(6):599–612. doi:10.1517/17425240902967607
13. Lee JA, Kim MK, Paek HJ, et al. Tissue distribution and excretion kinetics of orally administered silica nanoparticles in rats. *Int J Nanomedicine.* 2014;9:251–260. doi:10.2147/IJN.S57939
14. Wang C, Liu X, Chen S, Hu F, Sun J, Yuan H. Facile preparation of phospholipid–amorphous calcium carbonate hybrid nanoparticles: toward controllable burst drug release and enhanced tumor penetration. *Chem Commun.* 2018;54(93):13080–13083. doi:10.1039/C8CC07694D
15. Xiong H, Ni J, Jiang Z, Tian F, Zhou J, Yao J. Intracellular self-disassemble polysaccharide nanoassembly for multi-factors tumor drug resistance modulation of doxorubicin. *Biomater Sci.* 2018;6 (9):2527–2540. doi:10.1039/C8BM00570B
16. Yuan H, Chen J, Du YZ, Hu FQ, Zeng S, Zhao HL. Studies on oral absorption of stearic acid SLN by a novel fluorometric method. *Colloids Surf B Biointerfaces.* 2007;58:157–164. doi:10.1016/j.colsurfb.2007.03.002
17. Chai GH, Hu FQ, Sun JH, Du YZ, You J, Yuan H. Transport pathways of solid lipid nanoparticles across madin-darby canine kidney epithelial cell monolayer. *Mol Pharm.* 2014;11:3716–3726. doi:10.1021/mp5004674
18. Wang C, Li M, Yang T, et al. A self-assembled system for tumor-targeted co-delivery of drug and gene. *Mater Sci Eng C Mater Biol Appl.* 2015;56:280–285. doi:10.1016/j.msec.2015.06.034
19. Xiong H, Du S, Zhang P, Jiang Z, Zhou J, Yao J. Primary tumor and pre-metastatic niches co-targeting "peptides-lego" hybrid hydroxyapatite nanoparticles for metastatic breast cancer treatment. *Biomater Sci.* 2018;6(10):2591–2604. doi:10.1039/C8BM00706C
20. Guo J, Severtson SJ. Inhibition of calcium carbonate nucleation with aminophosphonates at high temperature, pH and ionic strength. *Ind Eng Chem Res.* 2004;43(17):5411–5417. doi:10.1021/ie049787i
21. Chen S-F, Colfen H, Antonietti M, Yu S-H. Ethanol assisted synthesis of pure and stable amorphous calcium carbonate nanoparticles. *Chem Commun.* 2013;49(83):9564–9566. doi:10.1039/c3cc45427d
22. Addadi L, Raz S, Weiner S. Taking advantage of disorder: amorphous calcium carbonate and its roles in biomineralization. *Adv Mater.* 2003;15(12):959–970. doi:10.1002/adma.200300381
23. Wan C-Q, Li A-M, Al-Thabaiti SA, El-Mosslamy E-SH, Mak TCW. Efficient solvent-controlled crystallization of pure polymorphs of 1-nitro-4-(4-nitrophenylmethylthio)benzene. *CrystEngComm.* 2014;16:8960–8968. doi:10.1039/C4CE00753K
24. Wang C, Han M, Liu X, et al. Mitoxantrone-preloaded water-responsive phospholipid-amorphous calcium carbonate hybrid nanoparticles for targeted and effective cancer therapy. *Int J Nanomedicine.* 2019;14:1503–1517. doi:10.2147/IJN.S193976
25. Yuan H, Lu LJ, Du YZ, Hu FQ. Stearic acid-g-chitosan polymeric micelle for oral drug delivery: in vitro transport and in vivo absorption. *Mol Pharm.* 2011;8:225–238. doi:10.1021/mp100289v

26. Sahay G, Alakhova DY, Kabanov AV. Endocytosis of nanomedicines. *J Control Release*. 2010;145(3):182–195. doi:10.1016/j.jconrel.2010.01.036

27. Matsubara T, Otani R, Yamashita M, Maeno H, Nodono H, Sato T. Selective intracellular delivery of ganglioside GM3-binding peptide through Caveolae/Raft-mediated endocytosis. *Biomacromolecules*. 2017;18(2):355–362. doi:10.1021/acs.biomac.6b01262

28. Durymanov MO, Beletkaia EA, Ulasov AV, et al. Subcellular trafficking and transfection efficacy of polyethylenimine-polyethylene glycol polyplex nanoparticles with a ligand to melanocortin receptor-1. *J Control Release*. 2012;163:211–219. doi:10.1016/j.jconrel.2012.08.027

29. Du WW, Fan YC, Zheng N, et al. Transferrin receptor specific nanocarriers conjugated with functional 7peptide for oral drug delivery. *Biomaterials*. 2013;34(3):794–806. doi:10.1016/j.biomaterials.2012.10.003

30. Mailander V, Landfester K. Interaction of nanoparticles with cells. *Biomacromolecules*. 2009;10:2379–2400. doi:10.1021/bm900266r

31. Rodriguez-Boulan E, Musch A, Le Bivic A. Epithelial trafficking: new routes to familiar places. *Curr Opin Cell Biol*. 2004;16(4):436–442. doi:10.1016/j.ceb.2004.06.013

32. Maxfield FR, McGraw TE. Endocytic recycling. *Nat Rev Mol Cell Biol*. 2004;5(2):121–132. doi:10.1038/nrm1315

33. Mikhail AS, Eetezadi S, Ekdawi SN, Stewart J, Allen C. Image-based analysis of the size- and time-dependent penetration of polymeric micelles in multicellular tumor spheroids and tumor xenografts. *Int J Pharm*. 2014;464(1–2):168–177. doi:10.1016/j.ijpharm.2014.01.010

34. Wong C, Stylianopoulos T, Cui JA, et al. Multistage nanoparticle delivery system for deep penetration into tumor tissue. *Proc Natl Acad Sci U S A*. 2011;108(6):2426–2431. doi:10.1073/pnas.1018382108

35. Liu Y, Ibricevic A, Cohen JA, et al. Impact of hydrogel nanoparticle size and functionalization on in vivo behavior for lung imaging and therapeutics. *Mol Pharm*. 2009;6(6):1891–1902. doi:10.1021/mp900215p

36. Wang J, Sui M, Fan W. Nanoparticles for tumor targeted therapies and their pharmacokinetics. *Curr Drug Metab*. 2010;11:129–141. doi:10.2174/138920010791110827

37. Natarajan A, Gruettner C, Ivkov R, et al. NanoFerrite particle based radioimmunonanoparticles: binding affinity and in vivo pharmacokinetics. *Bioconjug Chem*. 2008;19(6):1211–1218. doi:10.1021/bc800015n

38. Zhao X, Tang D, Yang T, Wang C. Facile preparation of biocompatible nanostructured lipid carrier with ultra-small size as a tumor-penetration delivery system. *Colloids Surf B Biointerfaces*. 2018;170:355–363. doi:10.1016/j.colsurfb.2018.06.017

39. Wang RN, Gu XC, Zhou JP, et al. Green design "bioinspired disassembly-reassembly strategy" applied for improved tumor-targeted anticancer drug delivery. *J Control Release*. 2016;235:134–146. doi:10.1016/j.jconrel.2016.05.055